




A validated modeling strategy for piezoelectric MEMS loudspeakers including viscous effects

Hamideh Hassanpour Guilvaiee^{1,*} , Paul Heyes² , Christian Novotny², Manfred Kaltenbacher³ , and Florian Toth¹ 

¹TUWien, Getreidemarkt 9, Objekt 1, 1060 Vienna, Austria

²USound GmbH, Gutheil-Schoder-Gasse 8-12, 1100 Wien, Austria

³TUGraz, Graz, Austria

Received 14 November 2022, Accepted 30 April 2023

Abstract – Piezoelectric micro-electro-mechanical system (MEMS) loudspeakers are drawing more interest due to their applications in new-developing audio technologies. MEMS devices' small dimensions necessitate including thermal and viscous effects in the surrounding air when simulating their behaviors. Thus, the linearized mass, momentum and energy conservation equations are used to describe these effects. These formulations are implemented in our open-source finite element program openCFS. In this article, we model a 3D piezoelectric MEMS loudspeaker in two configurations: open and closed back-volume, which behave differently due to the effects of air viscosity and pressure forces between the cantilever and the closed back-volume. Furthermore, using a customized vacuum chamber, the atmospheric pressure is varied and its effects are studied in these two configurations, numerically and experimentally. Experimental results prove that our model predicts the behavior of the piezoelectric MEMS loudspeaker in various configurations very well. Additional simulations illustrate the effect of the slit thickness and thermal losses.

Keywords: Piezoelectric MEMS loudspeakers, Finite element method, Thermoviscous acoustic

1 Introduction

MEMS loudspeakers are a new and rapidly developing field in electro-acoustics due to their potential applications in mobile devices, headphones, audio glasses and hearing aids. Most loudspeakers consist of an actuation mechanism, an acoustic diaphragm and an air chamber, therefore, to model them, multiple physical fields including solid mechanics, electrostatics and acoustics are involved. To excite the acoustic diaphragm, commonly utilized actuation mechanisms are piezoelectric, electrodynamic [1] and electrostatic [2]. In piezoelectric MEMS loudspeakers, a cantilever is excited by a piezoelectric layer sandwiched between two electrodes in the presence of the input alternating current (AC) voltage. These loudspeakers are becoming more popular because they require only a low voltage to provide a high actuation force [3] and are insensitive to dust [4].

The acoustic performance of a MEMS loudspeaker depends on material properties, structure and acoustic design. In MEMS loudspeakers, due to their small dimensions, care has to be taken into account for all relevant physical effects. Especially for modeling acoustics in the slit between the cantilever and the frame of the MEMS

loudspeaker, the thermal and viscous effects should be considered [5, 6]. For modeling thermal and viscous (thermoviscous) effects in the acoustic domain, various formulations are proposed [7–11] which carry the geometry restrictions. To avoid these geometry restrictions, we use the linearized thermoviscous acoustic formulation, which consists of the conservation of mass, momentum, and energy [11–13]. Although being computationally costly, this model fulfills both thermoviscous acoustic-solid coupling conditions i.e., continuity of velocity and continuity of traction.

Thermoviscous effects in MEMS were studied in various works. Naderyan et al. [14, 15] proposed an analytical solution based on the low reduced frequency for modeling thermoviscous acoustic damping in perforated MEMS. A further comparison to another finite element method (FEM) model showed good agreement between analytical and numerical solutions. In 2021, Liechti et al. [16] proposed lumped and FEM models for a piezoelectric MEMS loudspeaker, where they considered viscous losses between the frame and the plate. Later (in 2022), Massimino et al. [17] designed two MEMS speakers for an in-ear application considering thermoviscous damping.

In this work, we present a modeling strategy for piezoelectric MEMS loudspeakers. We use the FEM for solving the linearized conservation of mass, momentum and energy

*Corresponding author: hamideh.hassanpour@tuwien.ac.at

to take viscous and thermal effects into account. The formulation allows couplings to the flexible solid and the acoustic wave equation by using non-conforming interfaces [18]. Employing these formulations, we develop a 3D FEM model of a piezoelectric MEMS loudspeaker. After showing the importance of thermoviscous effects, the device is studied in closed and open back-volume configurations. Moreover, we study the effect of varying atmospheric pressure on the cantilever deflection. Furthermore, the device is experimentally tested in different configurations, namely with an open and closed back volume, respectively. This experimental data is then compared to the numerical simulations.

2 Physical modeling

Efficiently modeling a piezoelectric MEMS loudspeaker requires simulating various domains, including solid, piezoelectric, thermoviscous acoustics, and acoustic wave equation in the far-field. Figure 1 shows the topological sketch of these fields with their interfaces and boundaries.

2.1 Fluid governing equations

Acoustics in the thermoviscous domain Ω_{tv} is modeled by using the linearized form of the conservation of mass, momentum, and energy. This linearized formulation is obtained by applying perturbation ansatz and modeling the small fluctuations of velocity \mathbf{v} , pressure p , density ρ , and temperature T . In doing so, the total quantities are split into a steady background part $(\cdot)_0$ and a small perturbation part. In the frequency-domain modeling, the equations can be simplified by using the phasor representation. Using complex algebra, the acoustic perturbations pressure, velocity and temperature take the harmonic form of $pe^{i\omega t}$, $\mathbf{v}e^{i\omega t}$, and $Te^{i\omega t}$, respectively [19, 20]; a time derivative of any quantity ξ ($\frac{\partial \xi}{\partial t}$) becomes $i\omega\xi$. The final linearized conservation equations modeling the fluid behavior in the thermoviscous domain for these small perturbations are [18]

$$\frac{i\omega}{p_0}p + \nabla \cdot \mathbf{v} - \frac{i\omega}{T_0}T = 0 \quad \text{in } \Omega_{tv}, \quad (1a)$$

$$i\omega\rho_0\mathbf{v} - \nabla \cdot \boldsymbol{\sigma} = 0 \quad \text{in } \Omega_{tv}, \quad (1b)$$

$$i\omega\rho_0c_pT + \nabla \cdot \mathbf{q} - i\omega p = 0 \quad \text{in } \Omega_{tv}. \quad (1c)$$

Note that we assumed a fluid with the ideal gas behavior with no background velocity $\mathbf{v}_0 = 0$. Furthermore, the heat flux may be expressed by Fourier's law of heat conduction

$$\mathbf{q} = -\gamma_T \nabla T, \quad (2)$$

where γ_T is the thermal conductivity of air. The stress tensor $\boldsymbol{\sigma}$ for a Newtonian fluid is defined as

$$\begin{aligned} \boldsymbol{\sigma} &= -p\mathbf{I} + \boldsymbol{\tau} \\ &= -p\mathbf{I} + \mu(\nabla\mathbf{v} + (\nabla\mathbf{v})^T) + \left(\mu_b - \frac{2}{3}\mu\right)(\nabla \cdot \mathbf{v})\mathbf{I}, \end{aligned} \quad (3)$$

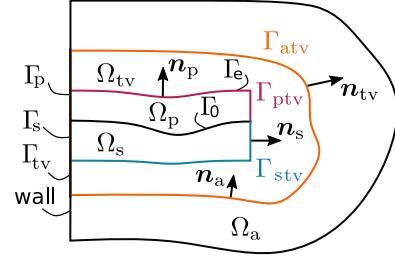


Figure 1. Sketch of the topology of a piezoelectric MEMS loudspeaker. We have piezoelectric Ω_p , flexible solid Ω_s , thermoviscous acoustic Ω_{tv} and acoustic Ω_a domains with their interfaces Γ_{stv} , Γ_{ptv} , Γ_{atv} . Boundary conditions are applied on solid (Γ_s), piezoelectric (Γ_p , Γ_e and Γ_0), and thermoviscous (Γ_{tv}) boundaries.

where viscous stress tensor, shear and bulk (or volume) viscosity are denoted with $\boldsymbol{\tau}$, μ and μ_b , respectively. Common boundary conditions in the thermoviscous acoustic domain are wall (where velocity and temperature are zero) and symmetry (where normal velocity is set to zero).

Solving the thermoviscous acoustic formulation with three unknowns is computationally costly and is only necessary when thermal and viscous boundary layers have significant effects (i.e., near walls). The thermal effects can be neglected in some cases. The resulting formulation includes the linearized conservation of mass and momentum with velocity and pressure degrees of freedom (dof) [21].

In regions where viscous and thermal boundary layers do not exist and their effects can be neglected, we use a linear acoustic wave equation

$$-\frac{\omega^2}{c^2}p_a - \nabla \cdot \nabla p_a = 0 \quad \text{in } \Omega_a, \quad (4)$$

where the speed of sound $c = \sqrt{K/\rho_0}$ is defined by the adiabatic compression modulus K , and the unperturbed acoustic density ρ_0 . The linear acoustic wave equation has one scalar unknown (pressure, p_a) and is computationally more efficient than thermoviscous acoustics formulations.

2.2 Solid and piezoelectric governing equations

The domain of the flexible solid Ω_s and the active piezoelectric material Ω_p are modeled by the conservation of momentum

$$-\omega^2\rho_i\mathbf{u} - \nabla \cdot \boldsymbol{\sigma}_i = \mathbf{0} \quad \text{in } \Omega_s \cup \Omega_p, \quad (5)$$

where index $i \in \{s, p\}$ is used to distinguish between flexible solid and active piezoelectric material, \mathbf{u} denotes the solid displacement, ρ_i the density of the solid/piezoelectric material, and $\boldsymbol{\sigma}_i$ is the stress tensor. We consider the material behavior in the solid domain as linear elastic but anisotropic, relating stress and strain tensor through the material stiffness tensor \mathbf{C} by

$$\boldsymbol{\sigma}_s = \mathbf{C} : \mathbf{s} \quad \text{in } \Omega_s, \quad (6)$$

where the solid strain \mathbf{s} is defined as

$$\mathbf{s} = \frac{1}{2}(\nabla \mathbf{u} + (\nabla \mathbf{u})^T). \quad (7)$$

At fixed walls (clampings) we enforce the homogeneous Dirichlet boundary condition ($\mathbf{u} = 0$).

In harmonic cases, with small perturbations from a reference state, the assumption of a linear constitutive law is valid. Therefore, in the piezoelectric domain, the linearized piezoelectric constitutive law is used

$$\boldsymbol{\sigma}_p = \mathbf{C} : \mathbf{s} - \boldsymbol{\epsilon} \cdot \mathbf{E} \quad \text{and} \quad \mathbf{D} = \boldsymbol{\epsilon} : \mathbf{s} + \boldsymbol{\epsilon} \cdot \mathbf{E} \quad \text{in } \Omega_p, \quad (8)$$

where $\boldsymbol{\epsilon}$ denotes the piezoelectric coupling tensor, \mathbf{E} and \mathbf{D} are the electric field and flux vectors, respectively, and $\boldsymbol{\epsilon}$ is the electric permittivity tensor. Furthermore, we use Gauss' law to describe the electric flux density by

$$\nabla \cdot \mathbf{D} = 0 \quad \text{in } \Omega_p, \quad (9)$$

and describe the electric field as $\mathbf{E} = -\nabla \phi$, where ϕ is the electric scalar potential. This identically fulfills Faraday's law for the electrostatic case, i.e. $\nabla \times \mathbf{E} = 0$. The Dirichlet boundary condition for an electric field is the electric potential $\phi = \phi_e$ and $\phi = 0$ at boundaries Γ_e and Γ_0 , respectively. The final linear piezoelectric formulations are obtained by inserting (8) into (5) and (9).

2.3 Coupling conditions

To model multiple domains, it is essential to ensure that the couplingS between them are enforced. A piezoelectric MEMS loudspeaker contains three couplings: solid-thermoviscous acoustics, acoustic-thermoviscous acoustic and piezoelectric-solid.

At the interface of the solid-thermoviscous acoustic coupled problem, one needs to enforce the dynamic and kinematic conditions requiring continuity of traction and velocity, respectively. Traction continuity (force equilibrium at the interface) is enforced by requiring

$$-\boldsymbol{\sigma} \cdot \mathbf{n}_{tv} = \boldsymbol{\sigma}_s \cdot \mathbf{n}_s \quad \text{on } \Gamma_{stv}, \quad (10)$$

where $\boldsymbol{\sigma}_s$ and $\boldsymbol{\sigma}$ are solid and thermoviscous stress tensors, respectively. The outwards facing normal vectors of solid \mathbf{n}_s and thermoviscous acoustics domains \mathbf{n}_{tv} are equal and opposite (see Fig. 1). The second condition (velocity continuity) is defined as

$$i\omega \mathbf{u} = \mathbf{v}. \quad (11)$$

At the interface of the acoustic-thermoviscous acoustic domains (Γ_{atv}) the dynamic and kinematic coupling conditions are applied. Thereby, the following transmission conditions along this interface (see Fig. 1) have to be fulfilled

$$\boldsymbol{\sigma} \cdot \mathbf{n} = -p_a \mathbf{n} = \boldsymbol{\sigma}_a \cdot \mathbf{n} \quad \text{on } \Gamma_{atv}, \quad (12)$$

$$\mathbf{v} \cdot \mathbf{n} = \mathbf{v}_a \cdot \mathbf{n} \quad \text{on } \Gamma_{atv}. \quad (13)$$

The continuity of pressure means that the net force should be zero on the (massless) interface separating the fluids.

Note that this coupling transmission is not valid where the viscous boundary layer exists. The continuity of the normal component of velocity implies that the fluid should stay in contact.

We assume region Ω_a to be modeled by the classical linear wave equation (assuming non-viscous fluid) and Ω_{tv} by the thermoviscous acoustic partial differential equations (PDEs). The normal vectors fulfill the following relation

$$\mathbf{n} = \mathbf{n}_{tv} = -\mathbf{n}_a. \quad (14)$$

3 Finite element formulations

The weak form of the problem serving as the basis for the finite element formulation is obtained by multiplying the test functions (denoted by (\prime)) to the governing PDEs, integrating over the computational domain, and applying integration by parts. Introducing p' and T' as the test functions of pressure and temperature, respectively, the weak forms of conservation of mass (1a) and of energy (1c) in the thermoviscous acoustic region are

$$i\omega \int_{\Omega_{tv}} \frac{1}{\rho_0} p' p \, d\Omega + \int_{\Omega_{tv}} p' \nabla \cdot \mathbf{v} \, d\Omega - i\omega \int_{\Omega_{tv}} \frac{1}{T_0} p' T \, d\Omega = 0, \quad (15a)$$

$$i\omega \int_{\Omega_{tv}} \rho_0 c_p T' T \, d\Omega + \int_{\Omega_{tv}} \gamma_T \nabla T' \cdot \nabla T \, d\Omega - i\omega \int_{\Omega_{tv}} T' p \, d\Omega + \int_{\Gamma_{tv}} T' \mathbf{q} \cdot \mathbf{n}_{tv} \, d\Gamma = 0. \quad (15b)$$

The thermoviscous acoustic normal vector \mathbf{n}_{tv} of the boundary Γ_{tv} points out of the thermoviscous acoustic domain Ω_{tv} (see Fig. 1). We use a polynomial basis function for the velocity that is one order higher than that used for the pressure. In the similar Stokes problem, this choice of polynomial orders fulfills the inf-sup (Ladyzhenskaya–Babuska–Brezzi (LBB)) condition. This condition is widely used in the Stoke equation to obtain well-posedness, ensuring that the elements do not lock and the pressure does converge.

To couple the acoustic wave equation with the thermoviscous acoustics formulation, we directly apply the dynamic (12) and the kinematic (13) transmission conditions into the weak form of thermoviscous acoustic conservation of momentum and the acoustic wave equation, respectively. The first transmission equation according to (12) can be written in the weak form by multiplying the velocity test function \mathbf{v}' and integrating over the interface Γ_{atv} . By doing so, the surface term in thermoviscous acoustics' conservation of momentum gets the form

$$\int_{\Gamma_{atv}} \mathbf{v}' \cdot \boldsymbol{\sigma} \cdot \mathbf{n} \, d\Gamma = - \int_{\Gamma_{atv}} \mathbf{v}' \cdot \mathbf{n} p_a \, d\Gamma, \quad (16)$$

where $\mathbf{n} = \mathbf{n}_{tv}$.

To apply the second transmission condition according to (13), we first derive the weak form of the wave equation

by multiplying the acoustic pressure test function p'_a to (4) and then integrating over the acoustic domain Ω_a . After applying Green's theorem, the weak form reads as

$$\int_{\Omega_a} \frac{1}{c^2} p'_a \frac{\partial^2 p_a}{\partial t^2} d\Omega + \int_{\Omega_a} \nabla p'_a \cdot \nabla p_a d\Omega - \int_{\Gamma_a} p'_a \mathbf{n}_a \cdot \nabla p_a d\Gamma = 0. \quad (17)$$

The conservation of momentum for acoustics in Ω_a (isentropic fluid) is

$$\nabla p_a = -\rho_0 \frac{\partial \mathbf{v}_a}{\partial t}. \quad (18)$$

This relation and the continuity of normal velocity in (13) allow us to rewrite the surface term in (17) as follows

$$\int_{\Gamma_{\text{atv}}} p'_a \mathbf{n}_a \cdot \nabla p_a d\Gamma = \int_{\Gamma_{\text{atv}}} \rho_0 p'_a \frac{\partial \mathbf{v}}{\partial t} \cdot \mathbf{n} d\Gamma, \quad (19)$$

where $\mathbf{n} = -\mathbf{n}_a$. Therefore, the final weak form of the acoustic wave equation in the frequency-domain is

$$\begin{aligned} -\omega^2 \int_{\Omega_a} \frac{1}{c^2} p'_a p_a d\Omega + \int_{\Omega_a} \nabla p'_a \cdot \nabla p_a d\Omega \\ - i\omega \int_{\Gamma_{\text{atv}}} \rho_0 p'_a \mathbf{v} \cdot \mathbf{n} d\Gamma = 0. \end{aligned} \quad (20)$$

For modeling thermoviscous acoustic-solid coupling, we applied a non-conforming symmetrization-free formulation [21]. This method does not introduce any other unknowns at the interface, such as those used in most of the Lagrange multiplier-based methods. Thus, it prevents saddle point problems in the discretized system. Also, since this method applies the coupling conditions in a weak sense, it can be used on non-conforming meshes, which are convenient for mesh generation. First, we apply the traction continuity condition (10) as

$$-\underbrace{\int_{\Gamma_{\text{stv}}} (\mathbf{u}' - \mathbf{v}') \cdot \boldsymbol{\sigma}_s \cdot \mathbf{n} d\Gamma}_{\text{traction consistency}}. \quad (21)$$

We keep the solid stress tensor for the simpler implementation since it contains only the displacement as an unknown. Second, we add the penalty term (*term penalty*) to guarantee the continuity of velocities

$$\underbrace{\beta \frac{p_e^2}{h_e} \int_{\Gamma_{\text{stv}}} (\mathbf{u}' - \mathbf{v}') \cdot \left(\frac{\partial \mathbf{u}}{\partial t} - \mathbf{v} \right) d\Gamma}_{\text{penalty}}. \quad (22)$$

This term is also known as the jump term. The normal direction of the interface \mathbf{n} is defined as $\mathbf{n} = \mathbf{n}_s = -\mathbf{n}_{\text{tv}}$. The penalty term contains the element order $p_e = \max(p_s, p_{\text{tv}})$ to account various polynomial orders, where, p_s and p_{tv} are the order of basis functions for solid and fluid domains, respectively. Furthermore, we add $1/h_e$ to the penalty term, where $h_e = \min(h_{\text{tv}}, h_s)$, i.e., the smallest element length of fluid or solid elements on the non-conforming interface [22].

Ultimately, the final version of thermoviscous acoustics conservation of momentum, including thermoviscous acoustics-solid and thermoviscous acoustics-acoustics couplings, in the frequency-domain is obtained as

$$\begin{aligned} i\omega \int_{\Omega_{\text{tv}}} \rho_0 \mathbf{v}' \cdot \mathbf{v} d\Omega + \int_{\Omega_{\text{tv}}} \nabla \mathbf{v}' : \boldsymbol{\sigma} d\Omega + \int_{\Gamma_{\text{atv}}} \mathbf{v}' \cdot \mathbf{n} p_a d\Gamma \\ - \int_{\Gamma_{\text{tv}}} \mathbf{v}' \cdot \boldsymbol{\sigma} \cdot \mathbf{n} d\Gamma + \underbrace{\int_{\Gamma_{\text{stv}}} \mathbf{v}' \cdot \boldsymbol{\sigma}_s \cdot \mathbf{n} d\Gamma}_{\text{traction consistency}} \\ - \underbrace{\beta \frac{p_e^2}{h_e} \int_{\Gamma_{\text{stv}}} \mathbf{v}' \cdot (i\omega \mathbf{u} - \mathbf{v}) d\Gamma}_{\text{penalty}} = \mathbf{0}. \end{aligned} \quad (23)$$

Additional boundary conditions are applied on the boundary Γ_{tv} .

In the solid domain Ω_s , the conservation of momentum (5) is the governing relation. In the piezoelectric domain Ω_p , Gauss' law (9) enters the formulations. After integration by parts and insertion of the relations (6) and (8) along with the coupling conditions (21) and (22) one obtains

$$\begin{aligned} -\omega^2 \int_{\Omega_s \cup \Omega_p} \mathbf{u}' \cdot \rho_i \mathbf{u} d\Omega \\ + \int_{\Omega_s \cup \Omega_p} \nabla \mathbf{u}' : \mathbf{C} : \mathbf{s} d\Omega + \int_{\Omega_p} \nabla \mathbf{u}' : \boldsymbol{\epsilon} \cdot \nabla \phi d\Omega \\ - \int_{\Gamma_s \cup \Gamma_p} \mathbf{u}' \cdot \boldsymbol{\sigma}_s \cdot \mathbf{n} d\Gamma - \underbrace{\int_{\Gamma_{\text{stv}}} \mathbf{u}' \cdot \boldsymbol{\sigma}_s \cdot \mathbf{n} d\Gamma}_{\text{traction consistency}} \\ + \underbrace{\beta \frac{p_e^2}{h_e} \int_{\Gamma_{\text{stv}}} \mathbf{u}' \cdot (i\omega \mathbf{u} - \mathbf{v}) d\Gamma}_{\text{penalty}} = \mathbf{0}, \end{aligned} \quad (24)$$

and

$$-\int_{\Omega_p} \nabla \phi' \cdot \boldsymbol{\epsilon} : \mathbf{s} d\Omega + \int_{\Omega_p} \nabla \phi' \cdot \boldsymbol{\epsilon} \cdot \nabla \phi d\Omega = 0, \quad (25)$$

where, solid and piezoelectric boundary conditions are applied on boundaries Γ_s and Γ_p , respectively. At the end, the final set of formulations used in modeling piezoelectric MEMS loudspeakers consists of (15a), (15b), (20), (23), (24) and (25).

4 Modeling of a piezoelectric MEMS loudspeaker

The investigated piezoelectric MEMS loudspeaker consists of a cantilever with a surface of $l_{\text{solid}} \times w_{\text{solid}}$, fixed to a rectangular frame on one side, schematically illustrated in Figure 2. This device is modeled in two configurations: open and closed back-volume indicated by orange and purple dashed lines where the back and front volumes are

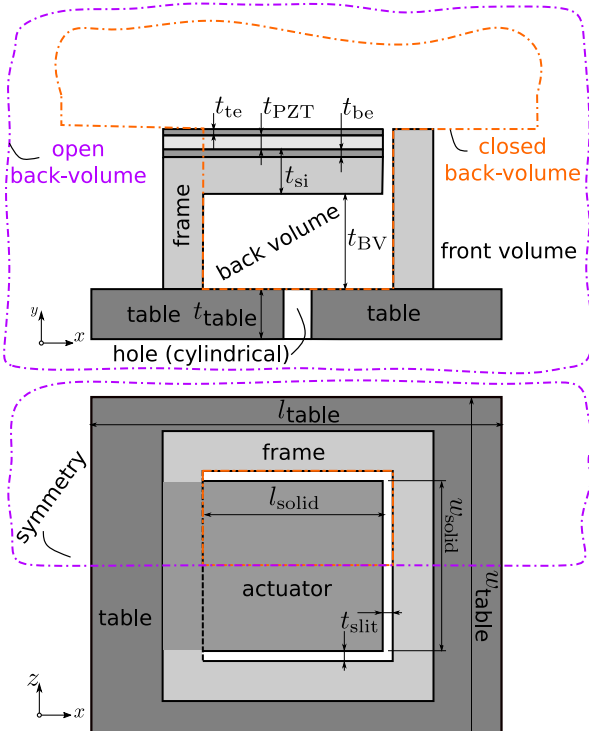


Figure 2. Section cut along the symmetry line and top view of the considered MEMS actuator (dimensions are not to scale). Orange and purple dashed lines indicate the closed and open back-volume simulation domains, where the back and front volumes are separated and connected (with a cylindrical hole), respectively.

connected and separated, respectively. The slit thickness (t_{slit}) between the cantilever and frame is $10 \mu\text{m}$. The active layer is made of lead zirconate titanate (PZT) with a thickness of t_{PZT} , sandwiched between two electrodes. Silicon (Si) is used as a passive layer and frame material. Silicon, top and bottom electrodes have a thickness of t_{Si} , t_{te} and t_{be} , respectively. The back volume has a height of t_{BV} . Tables 1, 2 and 3 describe the material properties of the different solid layers, air and piezoelectric material. Further piezoelectric MEMS loudspeaker's dimensions are provided in Table 4.

4.1 Numerical model

Finite element modeling of the device is performed using the open-source FEM code openCFS. The air between the frame and the plate (slit) is modeled using the thermoviscous acoustic formulation to capture the thermoviscous effects, whereas other acoustic regions are modeled using the acoustic wave equation. The free-field wave propagation is ensured using the perfectly matched layer (PML) domain around the front volume. The cantilever, which is clamped on one side, is excited using a potential difference of 0.2 V on the PZT layer. This excites the thermoviscous region and potentially causes wave propagation. Furthermore, the thermoviscous region around the slit ends with the wall boundary condition. Due to symmetry, half of the device is

Table 1. Solid material properties.

Property	Silicon	Top electrode	Bottom electrode
Density ρ in kg m^{-3}	2330	21 450	7700
Young's modulus E in Nm^{-2}	1.12×10^{11}	1.68×10^{11}	9.8×10^{10}
Poisson's ratio ν	0.28	0.38	0.23

Table 2. Air material properties.

Property	Air
Density ρ in kg m^{-3}	1.225
Bulk modulus K in N m^{-2}	1.4271×10^5
Dynamic viscosity μ in N s m^{-2}	1.829×10^{-5}
Bulk viscosity λ in N s m^{-2}	1.22×10^5
Adiabatic exponent κ	1.4
Specific heat capacity c_p in J K^{-1}	975.3
Thermal conductivity γ_T in W/(mK)	25.18×10^3

Table 3. Piezoelectric material properties.

Property	Piezoelectric material
Density ρ in kg m^{-3}	7600
Young modulus E in N m^{-2}	1.2×10^{11}
Poisson ratio ν	0.33
Permittivity ϵ in F m^{-1}	$\epsilon_{11} = \epsilon_{22}$ 2.771×10^{-8}
	ϵ_{33} 3.010×10^{-8}
Piezoelectric coupling tensor e in A s m^{-1}	$e_{31} = e_{32}$ -3.88
	$e_{24} = e_{15} = e_{33}$ 7.76

Table 4. Model dimensions.

Property	Value in μm
t_{te}	0.1
t_{PZT}	2.1
t_{be}	0.13
t_{si}	9.1
t_{BV}	280
t_{slit}	10
t_{table}	1000
l_{table}	200 000
w_{table}	300 000
w_{solid}	1680
l_{solid}	1680

simulated. Quadratic ansatz functions are used for thermoviscous acoustic velocity, temperature and solid displacement, whereas linear ansatz functions are used for pressure in thermoviscous acoustic and acoustic wave equations.

4.1.1 Closed back-volume

Figure 3 shows the geometry and mesh discretization of the closed back-volume piezoelectric MEMS loudspeaker. To model the wave propagation, a front volume with the

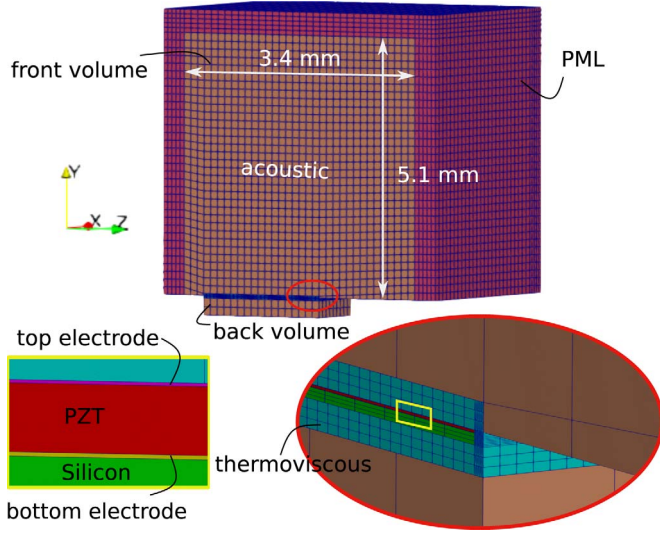


Figure 3. Mesh discretization for closed back volume.

size of $3360 \mu\text{m} \times 3360 \mu\text{m} \times 3360 \mu\text{m}$ is considered. The air is trapped in the back volume with dimensions of $1680 \mu\text{m} \times 1680 \mu\text{m} \times 280 \mu\text{m}$. Further, the PML domain is used to account for free radiation. The number of unknowns is stated in Table 5. Thermoviscous velocity has the most dof because first, polynomials of second order are used for velocity, and second, a finer mesh is used in the thermoviscous acoustic domain to resolve the viscous and thermal boundary layers correctly. On the thermoviscous-solid and thermoviscous-acoustic interfaces, non-conforming grids are used.

4.1.2 Open back-volume

In the open back-volume model, the back volume is connected to the front volume. To model this connection, a larger acoustic domain (in the size of the vacuum chamber) with the dimensions $2.55 \times 10^5 \mu\text{m} \times 4.1 \times 10^5 \mu\text{m} \times 3 \times 10^5 \mu\text{m}$ is connected to the closed back-volume acoustic domain using acoustic-acoustic non-conforming interfaces [23]. Figure 4 shows the mesh discretization in the open back-volume case. In this configuration, all domains except the acoustic domain remain the same as in the closed back-volume case (see Tab. 5). Moreover, the table where the device is placed on must be considered to avoid acoustic short circuits. This table and the frame of the device are considered as perfectly rigid domains; therefore, they have been left out while modeling. The dimensions of this table are given in Table 4.

4.1.3 Pressure variation

Changes in the atmospheric pressure affect the air behavior. Density and compression modulus are air material properties that vary for different pressures. The air compression modulus K varies for different pressure as

$$K = \kappa p_0, \quad (26)$$

Table 5. Degrees of freedom (dof) for open and closed back-volume configurations.

dof	Closed back-volume	Open back-volume
Solid mechanic displacement	194k	194k
Electric potential	10k	10k
Acoustic pressure	56k	712k
Temperature	794k	794k
Thermoviscous pressure	112k	112k
Thermoviscous velocity	2.3M	2.3M

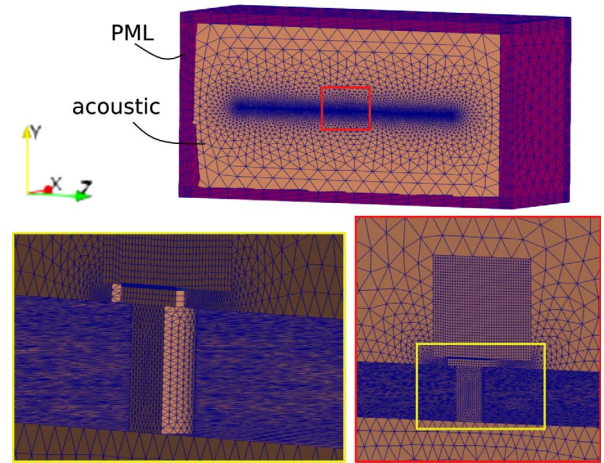


Figure 4. Mesh discretization for open back-volume.

where κ is the adiabatic exponent. Accordingly, the relation between air density and pressure is described using the ideal gas relation

$$\rho = \frac{p}{RT}, \quad (27)$$

where R is the ideal gas constant and is related to the adiabatic exponent as $R = c_p (1 - 1/\kappa)$. The viscosity of air has a temperature dependency, however, it does not vary significantly with atmospheric pressure.

4.2 Experimental setup

The model is validated against experimental results by comparing the produced sound pressure and the deflection amplitudes at different atmospheric pressures.

For the atmospheric pressure variation measurements, the devices are placed on a table inside a custom-designed vacuum chamber and electrically contacted using micropositioners (XYZ 300 TR, Quarter Research & Development, Bend, Oregon, USA). Double-sided adhesive tape is used to fix the frame of the sample to a surface inside the chamber, sealing off the back cavity. For open back-volume measurements, the sample is stuck above a small hole of roughly 1 mm in diameter in both the table surface and the adhesive tape, opening the back cavity up to the chamber volume. The chamber is evacuated using a Scroll-pump

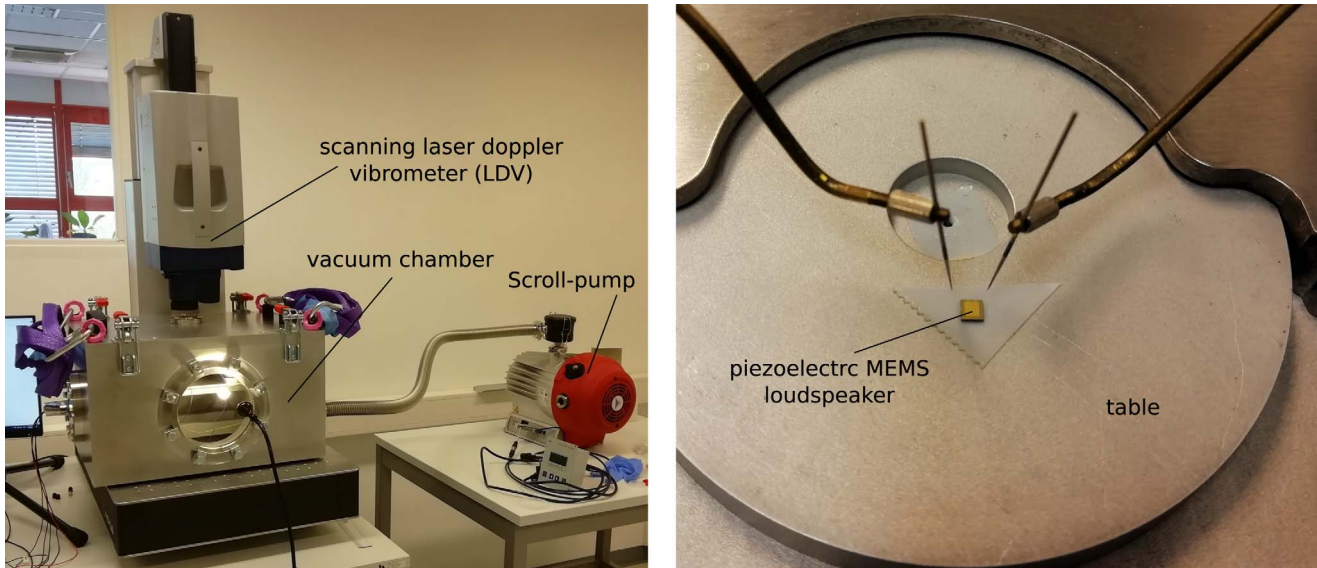


Figure 5. Experimental setup including the vacuum chamber, scanning laser doppler vibrometer (LDV), Scroll-pump and the MEMS loudspeaker inside the vacuum chamber.

(HiScroll 18, Pfeiffer Vacuum, Asslar, Germany) capable of reaching pressures down to 0.3 Pa. The chamber pressure is measured using the internal piezo/pirani-sensor of the scroll-pump (RPT010, Pfeiffer Vacuum, Asslar, Germany), with an accuracy of $\pm 15\%$ between 0.1 and 10 000 Pa, and ± 1500 Pa in the range from 10 000 Pa to atmospheric pressure. A chamber window above the device allows the plate deflection to be measured using a PSV-500 (Polytec, Waldbronn, Germany) scanning laser doppler vibrometer (LDV). Broad band anti-reflective coating (BBAR3) of the window mitigates reflective losses below 0.5% for wavelengths in the region of the HeNe-laser wavelength of the LDV. The setup is shown in [Figure 5](#). A periodic chirp signal ranging from 5 Hz to 32 kHz with an amplitude of 0.2 V peak AC and 0 V DC bias is applied. The velocity of the plate tip is measured at various pressures between 0.3 Pa and atmospheric pressure. A fast Fourier transform of the integrated measured time signal is performed using the LDV software PSV10.0 (Polytec, Waldbronn, Germany) yielding the deflection in the frequency domain. This is done both with a closed and open back-volume, measuring five samples to account for process variations in manufacturing.

The acoustic measurements are carried out with an APx515 System (Audio Precision, Beaverton, Oregon, USA) in conjunction with the measurement amplifier APx1701 (Audio Precision, Beaverton, Oregon, USA) and a free-field microphone GRAS 46BF (GRAS Sound and Vibration, Holte, Denmark). The devices are fixed far away from any reflecting obstacles in the closed back volume configuration, with the microphone positioned perpendicularly above the center of the plate at 13 distance, to maximize the signal-to-noise ratio (SNR) while still avoiding near-field effects. Frequency sweeps from 100 Hz to 30 kHz at 1 V peak AC are carried out, using the acoustic response function from the measurement software APx500 v5.0.3

(Audio Precision, Beaverton, Oregon, USA) to obtain the sound pressure level with respect to the frequency.

5 Simulation and experimental results

It is crucial to model the thermoviscous effects in MEMS loudspeakers due to their small dimension. To demonstrate the importance of these effects on the resonance frequency of the MEMS loudspeaker, we model the system with and without considering these effects. [Figure 6](#) compares the displacement of the cantilever in the acoustic domain with and without including thermoviscous effects. In the latter, the first resonance frequency of the cantilever is entirely damped. However, in the acoustic simulation, the resonance frequency of the system is observed at 4 kHz. The results are far from the actual physics of the solution when the thermoviscous effects are neglected.

5.1 Closed back-volume

[Figure 7](#) shows the cantilever deflection at the frequency of $f = 3.7$ kHz and 100 kPa, where the solid layers are excited by a 0.2 V potential. The MEMS cantilever shows the expected bending type deformation of the first resonance. The displacement at the tip of the cantilever (marked in [Fig. 7](#)) is plotted over frequency (1–20 kHz) in [Figure 6](#). This figure also displays the experimental results for the different samples and their two standard deviations. The simulation results are within this deviation up to 17.5 kHz. Both experimental and simulation results indicate that the peak at the first resonance of the cantilever (at 4 kHz) is damped due to the viscosity of the air.

The acoustic pressure field and sound pressure level (SPL) at the distance of 13 mm are shown in more detail in [Figures 8a](#) and [8b](#), respectively. [Figure 8a](#) indicates the

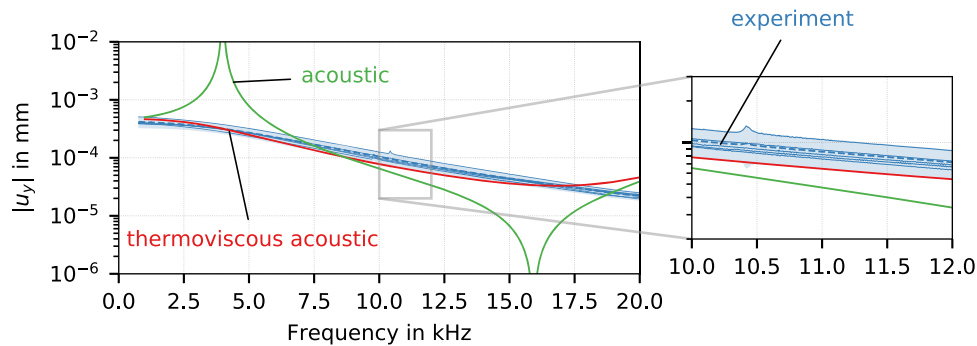


Figure 6. Displacement at the tip of the cantilever in two cases: with and without thermoviscous effects at 100 kPa with excitation of 0.2 V. The experimental results are shown as mean (dashed line) $\pm 2\sigma$ (shaded region) using the standard deviation σ of the 5 individual measurements (full thinner lines).

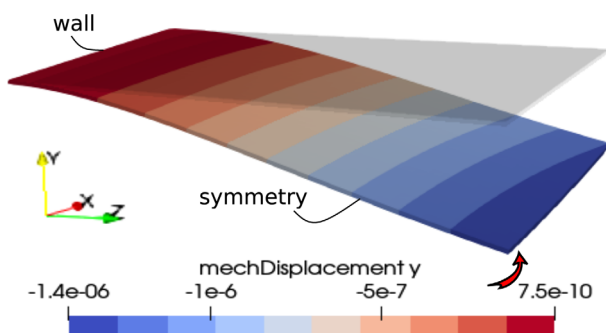
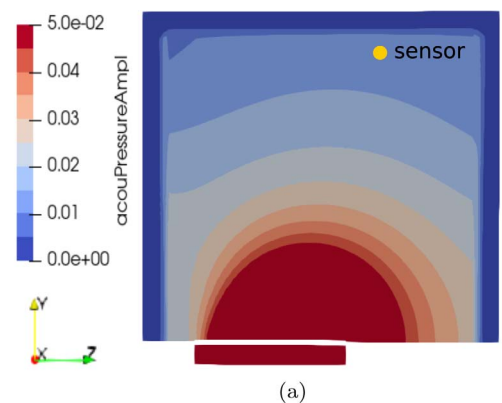


Figure 7. MEMS loudspeaker's cantilever deformation in closed back-volume at 100 kPa with excitation of 0.2 V at $f = 3.8$ KHz.

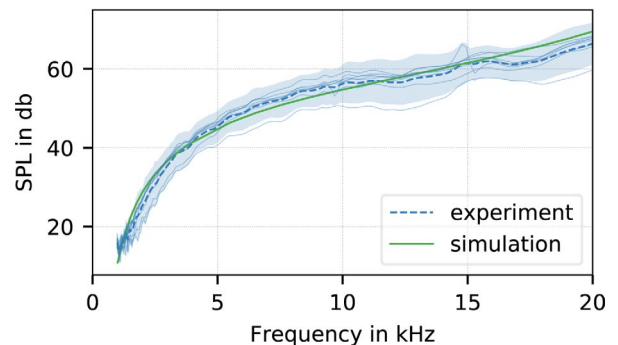
acoustic pressure amplitudes are radially decaying. The PML region damps the wave and simulates far-field wave propagation. Note that further simulations with a larger acoustic domain exhibit similar behaviors. Figure 8b shows the experimental and numerical SPL, which agree within two standard deviations of the experimental data up to 20 kHz. Furthermore, a SPL of 55 dB is achieved at the frequency of 5 kHz, which is promising considering the loudspeaker's small dimensions.

Furthermore, we have studied the effect of atmospheric pressure on the cantilever displacement. Figure 9 demonstrates the experimental and numerical displacements at the tip of the cantilever for four atmospheric pressure of 1000, 2800, 32 000 and 100 000 Pa with an excitation of 0.2 V in the closed back-volume configuration. A confidence belt ($\pm 2\sigma_i$) for the measurement results is obtained by taking into account the standard deviations (σ_i) of the peak location (first natural frequency) and amplitude variation. The mean amplitude of the experimental results was obtained after frequency-shifting to the mean peak location frequency. Figure 9 shows that the simulation results can reasonably predict the first resonance frequencies and are between the experimental deviations up to 11 kHz.

At lower pressure, the damping effects are low; therefore, the resonances are sharper with higher amplitudes



(a)



(b)

Figure 8. Pressure field and SPL in the closed back-volume configuration with an excitation of 1 V at an atmospheric pressure of 100 kPa. (a) Acoustic pressure field at $f = 5$ kHz. (b) Sound pressure level (SPL) at distance of 13 mm. The experimental results are shown as mean (dashed line) $\pm 2\sigma$ (shaded region) using the standard deviation σ of the 8 individual measurements (full thinner lines).

and closer to the natural resonance frequency of the cantilever. Increasing the pressure causes more damping and fades out the resonance peaks. This damping is related to two reasons: air viscosity and air pressure forces between the cantilever and closed back-volume [24]. This pressure force results in an increase in the stiffness of the cantilever

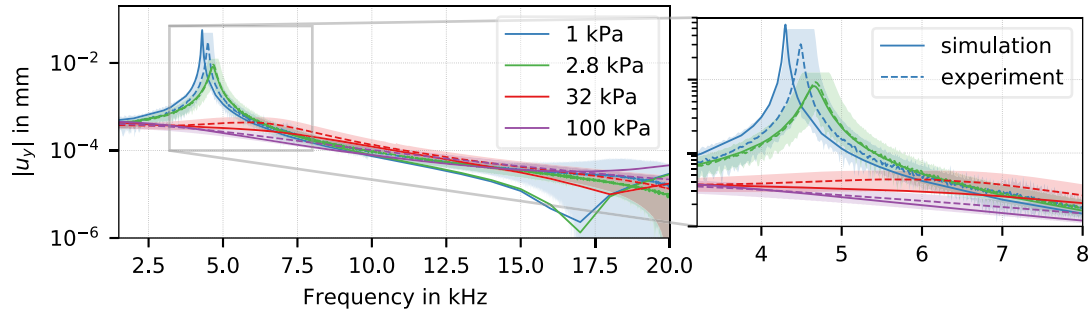


Figure 9. Displacement at the tip of the cantilever in the closed back-volume configuration at various atmospheric pressures of 1, 2.8, 32 and 100 kPa. The shaded region indicates the statistical variation on the experimental results ($\pm 2\sigma$) by taking into account the standard deviation of the peak location (first natural frequency) and amplitude variation. The mean amplitude of the experimental results (obtained after frequency-shifting to the mean peak location frequency) is shown as a dashed line.

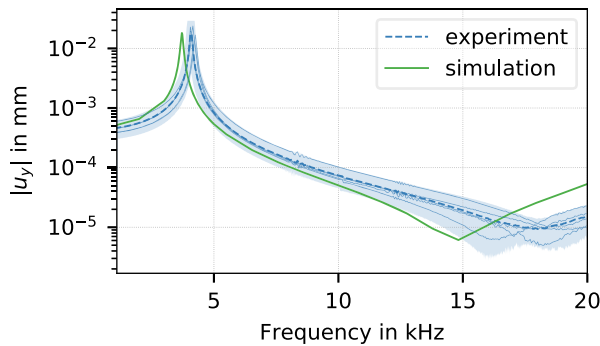


Figure 10. Displacement at the tip of the cantilever with an excitation of 0.2 at an atmospheric pressure of 100 in the open back-volume configuration. The shaded region indicates the statistical variation on the experimental results ($\pm 2\sigma$) by taking into account the standard deviation of the peak location (first natural frequency) and amplitude variation. The mean amplitude of the experimental results (obtained after frequency-shifting to the mean peak location frequency) is shown as a dashed line. The 5 measurements are plotted as dotted lines.

and consequently shifts in resonance frequency [25, 26]. Figure 9 shows that resonances are shifted to higher frequencies at higher pressure, where higher pressure force and subsequently higher stiffness exist.

5.2 Open back-volume

In the open back-volume, the back volume is connected to the front volume; therefore, air is no longer trapped in the back volume. Figure 10 shows the displacement at the tip of the cantilever over the frequency range of 1–20 kHz with an excitation of 0.2 V at an atmospheric pressure of 100 kPa. Although the resonance peak is slightly before the confidence band, the shape of the curve agrees remarkably well. The displacement amplitude is within two standard deviations for a wide frequency range from 5 to 13 kHz. In contrast to the closed back-volume case, the cantilever shows its first resonance at a frequency of ~ 4 kHz.

The acoustic pressure field is shown in Figure 11 at a frequency of 5 kHz and an atmospheric pressure of 100 kPa.

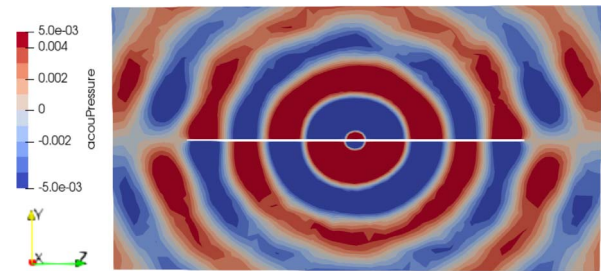


Figure 11. Pressure field at 100 kPa and $f = 5$ kHz with an excitation of 1 V in open back-volume configuration.

The radially decaying waves with their dipole character are visible.

Moreover, the effect of the atmospheric pressures is shown in Figure 12. This figure shows the displacement at the tip of the cantilever over different atmospheric pressures of 3, 60 and 100 kPa. The air viscosity and compression damping in the open back-volume are not as pronounced as in the closed back-volume configuration. In the open back-volume configuration, the system shows its resonance frequency in all the atmospheric pressures at ~ 4 kHz. Similar to the closed back-volume configuration, lower displacement amplitudes are achieved at higher pressures due to viscous damping, and sharper peaks with larger displacement amplitudes are observed at lower pressures. Counter to the closed back-volume configuration, the resonances are shifted to lower frequencies with increasing atmospheric pressure. Since the damping effect is weak in the open back-volume configuration, atmospheric pressure only affects the air density. Therefore, by increasing the pressure, the air density increases (added mass effect) and causes lower resonances. While the amplitude curves agree well with the averaged experimental results (in terms of shape and amplitude values), the model consistently under-predicts the first natural frequency in this case.

5.3 Impact of the slit thickness

The slit thickness is one of the critical design parameters in the closed back-volume MEMS loudspeaker, since

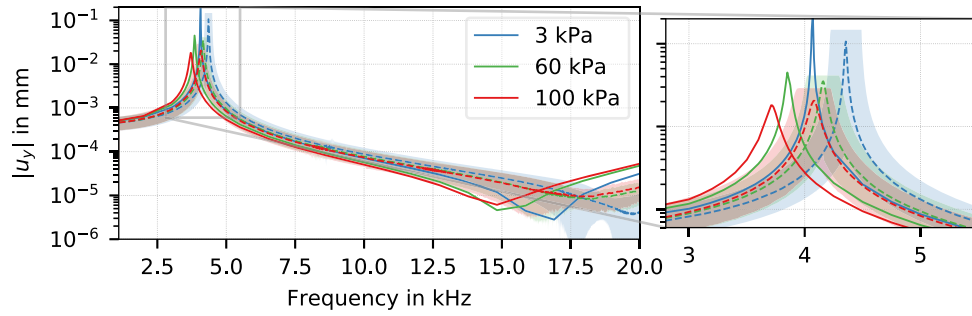


Figure 12. Displacement at the tip of the cantilever at different atmospheric pressures of 3, 60 and 100 kPa with an excitation of 0.2 V in the open back-volume configuration. The shaded region indicates the statistical variation on the experimental results ($\pm 2\sigma$) by taking into account the standard deviation of the peak location (first natural frequency) and amplitude variation. The mean amplitude of the experimental results (obtained after frequency-shifting to the mean peak location frequency) is shown as a dashed line.

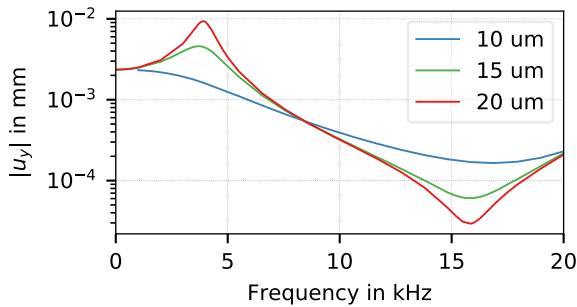


Figure 13. Displacement at the tip of the cantilever using different slit thicknesses of 10, 15 and 20 μm in the closed back-volume configuration with an excitation of 0.2 V and the atmospheric pressure of 100 kPa.

it significantly affects the viscous damping and resonance frequencies of the system. The slit thickness which was originally set to 10 μm , is further varied to 15 μm and 20 μm . The displacements at the tip of the cantilever over frequency, using these slit thicknesses, are plotted in Figure 13. These studies are done at the atmospheric pressure of 100 kPa with the excitation of 0.2 V. A narrower slit thickness causes higher damping and fades out the displacement peak. By increasing the slit thickness, higher displacements with sharper peaks are observed. The resonances are slightly shifted to higher frequencies due to the damping effect discussed previously.

5.4 Importance of thermal effect

The study of thermal effects is important since eliminating the temperature dof can significantly reduce computational effort. Therefore, we model the piezoelectric MEMS loudspeaker with and without thermal effects using thermoviscous acoustic and viscous acoustic formulations, respectively. Figures 14 and 15 show the displacement at the tip of the cantilever and acoustic pressure in the frequency range of 1–5 kHz at a distance of 3.2 mm with an excitation of 0.2 V and the atmospheric pressure of 100 kPa in closed and open back-volume configuration, respectively. These figures demonstrate that in both open and closed

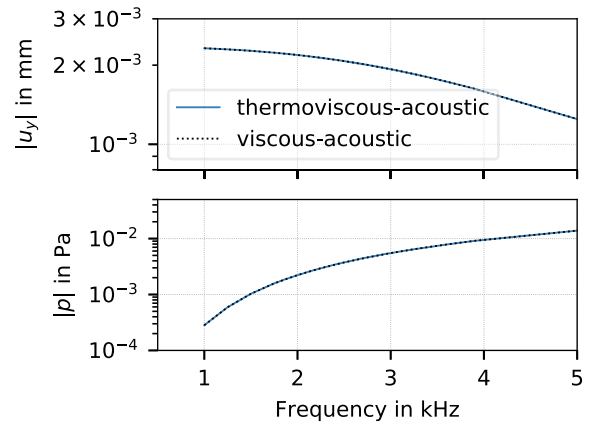


Figure 14. Displacement at the tip of the cantilever and acoustic pressure at a distance of 3.2 mm for the closed back-volume case.

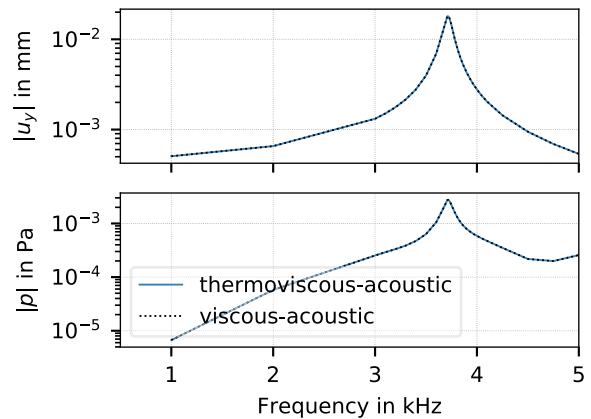


Figure 15. Displacement at the tip of the cantilever and acoustic pressure at a distance of 3.2 mm for the open back-volume case.

back-volume configurations, cantilever displacement and acoustic pressure are equal with and without thermal effects. This leads to a reduction of 794k dof for temperature and

reduces the solution time by 37% and 42% for closed and open back-volume configurations, respectively.

6 Conclusion

In this work, we modeled a 3D piezoelectric MEMS loudspeaker using our open source finite element program, which includes thermoviscous effects. Furthermore, we conducted experiments in various configurations to validate this model. We studied these effects in closed and open back-volume configurations (where the back and front volumes are separated and connected, respectively) at various atmospheric pressures. A customized vacuum chamber was used to vary the atmospheric pressure in the experimental setup. In the closed back-volume case, thermoviscous effects altered the cantilever's displacements and consequently the SPL, and faded out the cantilever's first resonance at ~4 kHz. The numerical results, displacement, and SPL agreed well with the experimental data. In the open back-volume case, the damping effects are not as pronounced as for the closed back-volume. Therefore, the first resonance frequency is still at ~4 kHz, which is verified with experimental displacements.

The cantilever displacement amplitudes were affected by altering the atmospheric pressure. In the closed and open back-volume configurations, increasing pressure causes more damping and lower displacement amplitudes. Regarding the cantilever displacements, experimental results also captured the same behavior. Displacement peaks were sharper at lower pressure. Unlike the open back-volume case, the resonances shifted to higher frequencies for the closed back-volume. This is due to an increase in the stiffness of the cantilever as a consequence of the compression force between the cantilever and closed back-volume. In the open back-volume configuration, the resonances slightly shifted to lower frequencies when increasing pressure and subsequently increasing the density.

Furthermore, the slit thickness was studied. Using three different configurations with a thickness of 10, 15, and 20 μm showed that increasing the slit thickness caused lower damping and, therefore, higher and sharper displacement peaks. Moreover, we showed that the thermal effects are negligible. This reduced the computation time by ~40%. In conclusion, this validated method and simulation strategy can be used for modeling similar MEMS devices.

Conflict of interest

The authors declare no conflict of interest.

Acknowledgments

This work was partly funded by the Austrian Research Promotion Agency (FFG) within the program line "Bridge" (project number 868033). The authors acknowledge TU Wien Bibliothek for financial support through its Open Access Funding Programme.

References

1. E. Sturtzer, I. Shahosseini, G. Pillonnet, E. Lefevre, G. Lemarquand: High fidelity microelectromechanical system electrodynamic micro-speaker characterization. *Journal of Applied Physics* 113, 21 (2013) 214905.
2. M. Vikas Garud, R. Pratap: A novel MEMS speaker with peripheral electrostatic actuation. *Journal of Microelectromechanical Systems* 29, 4 (2020) 592–599.
3. I.J. Cho, S. Jang, H.J. Nam: A piezoelectrically actuated MEMS speaker with polyimide membrane and thin film pb (zr, ti)o₃(pzt) actuator. *Integrated Ferroelectrics* 105, 1 (2009) 27–36.
4. R. Dejaeger, F. Casset, B. Desloges, G. Le Rhun, P. Robert, S. Fanget, Q. Leclère, K. Ege, J.L. Guyader: Development and characterization of a piezoelectrically actuated MEMS digital loudspeaker. *Procedia Engineering* 47 (2012) 184–187.
5. T. Vejjola, M. Turowski: Compact damping models for laterally moving microstructures with gas-rarefaction effects. *Journal of Microelectromechanical Systems* 10, 2 (2001) 263–273.
6. W.M. Beltman: Viscothermal wave propagation including acousto-elastic interaction, Part I: Applications. *Journal of Sound and Vibration* 227, 3 (1999) 587–609.
7. A. Trochidis: Vibration damping due to air or liquid layers. *Acustica* 51, 4 (1982) 201–212.
8. R. Bossart, N. Joly, M. Bruneau: Hybrid numerical and analytical solutions for acoustic boundary problems in thermo-viscous fluids. *Journal of Sound and Vibration* 263, 1 (2003) 69–84.
9. M. Berggren, A. Bernland, D. Noreland: Acoustic boundary layers as boundary conditions. *Journal of Computational Physics* 371 (2018) 633–650.
10. W.M. Beltman: Viscothermal wave propagation including acousto-elastic interaction. PhD thesis, University of Twente, 1998.
11. M.J.J. Nijhof: Viscothermal wave propagation. PhD thesis, Universiteit Twente, 2010.
12. W.R. Kampinga, Y.H. Wijnant, A. de Boer: An efficient finite element model for viscothermal acoustics. *Acta Acustica United with Acustica* 97, 4 (2011) 618–631.
13. W.R. Kampinga, Y.H. Wijnant, A. de Boer: Performance of several viscothermal acoustic finite elements. *Acta Acustica United with Acustica* 96, 1 (2010) 115–124.
14. V. Naderyan, R. Raspet, C. Hickey, M. Mohammadi: Analytical and computational modeling of viscothermal acoustic damping in perforated microstructures, in: 23rd International Congress on Acoustics, September, 2019, pp. 7580–7585.
15. V. Naderyan, R. Raspet, C. Hickey: Thermo-viscous acoustic modeling of perforated micro-electro-mechanical systems (MEMS). *Journal of the Acoustical Society of America* 148, 4 (2020) 2376–2385.
16. R. Liechti, S. Durand, T. Hilt, F. Casset, C. Dieppedale, T. Verdot, M. Colin: A piezoelectric MEMS loudspeaker lumped and FEM models, in 2021 22nd International Conference on Thermal, Mechanical and Multi-Physics Simulation and Experiments in Microelectronics and Microsystems, EuroSimE 2021, 2021.
17. G. Massimino, C. Gazzola, V. Zega, S. Adorno, A. Corigliano: Ultrasonic piezoelectric MEMS speakers for in-ear applications: bubbles-like and pistons-like innovative designs, in: International Conference on Thermal, Mechanical and Multi-Physics Simulation and Experiments in Microelectronics and Microsystems (EuroSimE), IEEE, 2022, pp. 2–5.

18. F. Toth, H.H. Guilvaiee, G. Jank: Acoustics on small scales: Modelling viscous effects in MEMS devices. *Elektrotechnik und Informationstechnik*. 2021.
19. J.N. Reddy, D.K. Gartling: *The finite element method in heat transfer and fluid dynamics*. 3rd ed., Springer, 2010.
20. N. Joly: Finite element modeling of thermoviscous acoustics on adapted anisotropic meshes: Implementation of the particle velocity and temperature variation formulation. *Acta Acustica United with Acustica* 96, 1 (2010) 102–114.
21. H.H. Guilvaiee, F. Toth, M. Kaltenbacher: A non-conforming finite element formulation for modeling compressible viscous fluid and flexible solid interaction. *International Journal for Numerical Methods in Engineering* July (2022) 1–21.
22. A. Fritz, S. Hieber, B.I. Wohlmuth: A comparison of mortar and Nitsche techniques for linear elasticity. *Calcolo* 41, 3 (2004) 115–137.
23. M. Kaltenbacher, S. Floss: Nonconforming finite elements based on nitsche-type mortaring for inhomogeneous wave equation. *Journal of Theoretical and Computational Acoustics* 26, 3 (2018) 1–18.
24. M. Bao, H. Yang: Squeeze film air damping in MEMS. *Sensors and Actuators, A: Physical* 136, 1 (2007) 3–27.
25. A. Dantan: Membrane sandwich squeeze film pressure sensors. *Journal of Applied Physics* 128, 9 (2020) 091101.
26. S. Naserbakht, A. Dantan: Squeeze film pressure sensors based on SiN membrane sandwiches. *Sensors and Actuators, A: Physical* 298 (2019) 1–9.

Cite this article as: Hassanpour Guilvaiee H. Heyes P. Novotny C. Kaltenbacher M. & Toth F, 2023. A validated modeling strategy for piezoelectric MEMS loudspeakers including viscous effects. *Acta Acustica*, 7, 24.